12216 *J. Phys. Chem. A* **2007,** *111,* 12216−12228

Angular Distributions for Vibrationally Inelastic Nonresonant Scattering of Electrons by Molecules[†]

Petr Čársky,*,[‡] Roman Čurík,[‡] Barbara Pezler,[‡,§] and Josef Michl[‡,£]

*J. Heyrovský Institute of Physical Chemistry, Academy of Sciences of the Czech Republic, v.v.i.,
Dolejškova 3, 18223 Prague 8, Czech Republic, Faculty of Science, University of Podlesie,
ul. 3. Mája 54, 08-110 Siedlce, Poland, and Department of Chemistry and Biochemistry,
University of Colorado, Boulder, Colorado 80309-0215*

Received: May 23, 2007; In Final Form: August 6, 2007

Polar graphs for differential cross section (dcs) called spatial dcs maps are presented as graphical representation of the angular distribution of vibrationally inelastic electron scattering by polyatomic molecules. The objective of this paper is to show that an intuitive understanding of the principal features of these graphs can be obtained from a simple analysis of the normal modes of vibration of the target molecule and plane-wave functions representing the scattering electron. The procedure is illustrated on the H_2 and CH_4 molecules.

1. Introduction

The title of this paper has been intentionally selected as a counterpart to the title of F. H. Read's pioneering paper[1] "Angular Distributions for Resonant Scattering of Electrons by Molecules". Indeed, since the early attempts[2−6] to explain and predict angular distributions of vibrational excitation of molecules by electron impact, attention has been focused on resonant scattering, as illustrated by more recent applications (see, for example, refs 7−9) and by a recent comprehensive review.[10] In this paper, we concentrate on nonresonant scattering. More precisely, since resonant and nonresonant scattering cannot be rigorously distinguished, we deal with electron scattering at energies that do not correspond to shape resonances. In our application of the static exchange approximation to H_2 and H_2O molecules,[11] lacking explicit interaction with resonant states, the resonances are still reproduced to some extent, though, in the calculated energy dependence of the integral vibrational cross section, the maxima corresponding to resonances are underestimated and shifted to higher energies. Hence, it seems to us that a theory based on symmetry arguments for nonresonant scattering can be a good starting point for a future development of a unified theory for both resonant and nonresonant scattering. The objective of this paper is to demonstrate how the principal features of the angular distribution of vibrationally inelastic scattering can be deduced from simple consideration of symmetry and the form of normal modes without reference to the full complexity of the quantitative tools of scattering theory.

Thus, we are not trying to devise an approximate method for the calculation of the angular dependence of vibrationally inelastic scattering cross sections that would replace the full-blown complex static exchange ab initio calculation. Rather, we are reporting that it is possible to understand qualitatively and in simple intuitive terms the results of such computations, and we illustrate the procedure on H_2 and CH_4. Since the full static exchange calculations are already known to agree with experimental data for energies higher than about 8 eV (see, for example, refs 10,12), we do not need to address a comparison with experiment here. It is conceivable that the simple analysis devised here might provide useful predictions for larger molecules as well, and we intend to examine this possibility elsewhere.

For infrared (IR)-active modes, a simple rule is available according to which forward scattering dominates.[13] Here, we treat IR-inactive modes, that is, modes with a zero derivative of the dipole moment with respect to the normal coordinate.

2. Theory

2.1. Spatial Differential Cross Section Maps. For graphical representation of the angular distribution of vibrationally inelastic electron scattering, we use graphs called spatial differential cross section (dcs) maps. These are three-dimensional polar plots of differential cross sections. The $\mathbf{k}_1$ vector for the incoming electron is fixed along a selected significant direction in the molecular framework, for example, parallel or perpendicular to a principal molecular axis or parallel to a bond. The value of the differential cross section is plotted along the direction of the $\mathbf{k}_2$ vector, which describes the direction of the outgoing electron. The spatial dcs maps are constructed using the formula

$$D_{ji} = \sum_{lm} \sum_{l'm'} A_{lm,l'm'} Y^{*}_{lm}(\hat{\mathbf{k}}_j) Y_{l'm'}(\hat{\mathbf{k}}_i) \qquad (1)$$

which represents a transformation of the dcs from the plane-wave basis to the basis of spherical harmonics. The differential cross section D_{ji} is defined as the probability for the electron scattering $\mathbf{k}_i \rightarrow \mathbf{k}_j$. The coefficients $A_{lm,l'm'}$ can be derived from eq 1 as

$$A_{lm,l'm'} = \sum_{j} \sum_{i} w_j w_i Y_{lm}(\hat{\mathbf{k}}_j) Y^{*}_{l'm'}(\hat{\mathbf{k}}_i) D_{ji} \qquad (2)$$

where w_i and w_j are weights in the angular quadrature. Solution of the Lippmann−Schwinger equation by numerical

---

[†] Part of the "Giacinto Scoles Festschrift".

* To whom correspondence should be addressed. E-mail: carsky@jh-inst.cas.cz.

[‡] Academy of Sciences of the Czech Republic.

[§] University of Podlesie.

[£] University of Colorado.

10.1021/jp073981b CCC: $37.00

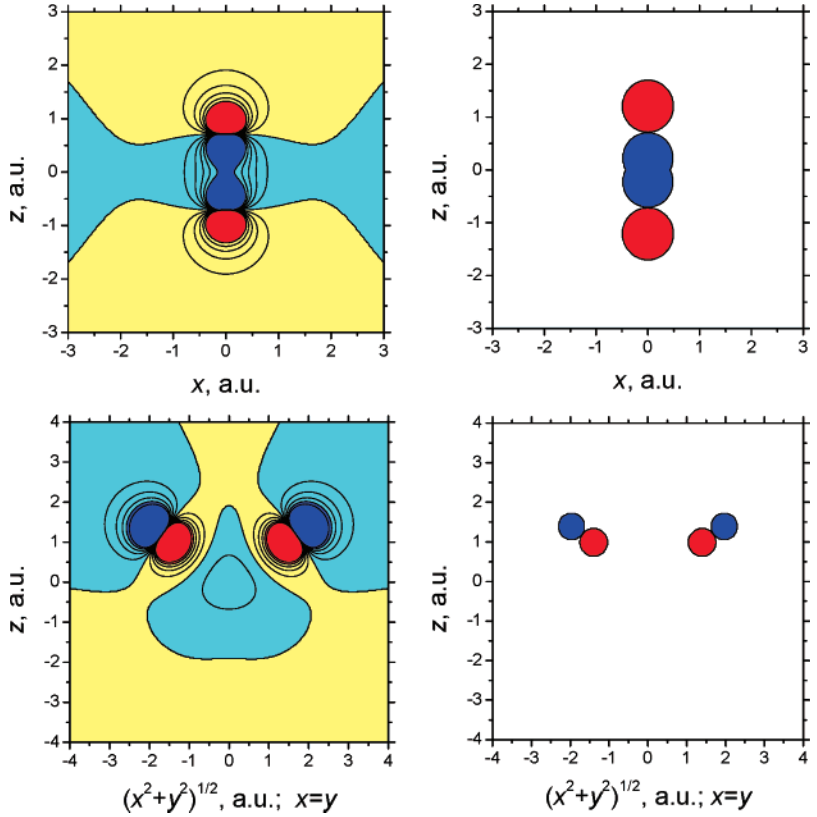

Figure 1. Maps of derivative of the electrostatic potential of H_2 with respect to the normal coordinate in the σ_{xz} plane (top) and of CH_4 with respect to the symmetric stretching normal coordinate in the H(3)−C−H(4) plane (bottom). The maps on the left were calculated rigorously, and those on the right were simulated by means of eq 6. Red and yellow mark regions of positive values, and blue regions mark those with negative values. The step in contours is 0.1.

quadrature yields the differential cross section for a definite number of pairs of $\mathbf{k}_1$ and $\mathbf{k}_2$ vectors as given by the angular quadrature.[11] These are used for obtaining $A_{lm,l'm'}$ coefficients from eq 2. Once the $A_{lm,l'm'}$ values are available, the dcs can be evaluated for any pair of $\mathbf{k}_1$ and $\mathbf{k}_2$ by means of eq 1. As is apparent from figures in the next sections, the spatial dcs maps exhibit distinct anisotropy. We will show that the main features of spatial dcs maps can be estimated without scattering calculations and evaluation of $A_{lm,l'm'}$ coefficients by means of simple considerations based on symmetry arguments alone.

2.2. Approximate T_{10} Maps. As with transition moments in photon spectroscopy, we require that the integrand of the amplitude $-2\pi^2 <\chi_1 k_1|T|\chi_0 k_0>$ for the 1 ← 0 vibrational excitation be totally symmetric. In the two-channel approximation, the T operator is given[11] by the Lippmann−Schwinger equation as

$$T_{10} = U_{10} + U_{10}G_0T_{00} + U_{11}G_1T_{10} \tag{3}$$

$$T_{00} = U_{00} + U_{00}G_0T_{00} + U_{01}G_1T_{10} \tag{4}$$

where the subscripts 10 and 00 refer to the transitions 1 ← 0 and 0 ← 0, respectively. Since the Green's functions G_0 and G_1 are totally symmetric, the symmetry of the T_{10} operator is determined by the symmetry of U_{10}. If the harmonic approximation is adopted, U_{10} for the ith normal mode can be taken[11] as the derivative of the electron−molecule interaction potential with respect to the ith dimensionless normal coordinate

$$U_{10} = (1/\sqrt{2})\ \partial U/\partial q_i \tag{5}$$

Hence, the symmetry of T_{10} is the same as that of q_i. For qualitative estimates, we may neglect the exchange term in the interaction potential U and construct U_{10} from the static potential U_s alone. U_s can be easily obtained from standard quantum chemical software. Commonly used programs such as Gaussian[14] or Hondo[15] have an option that permits a calculation of electrostatic potential maps. By calculating electrostatic potential maps at geometries displaced by $+\Delta q_i$ and $-\Delta q_i$ along the ith vibrational coordinate, we can obtain the numerical derivative $\Delta U_s/\Delta q_i$, which when multiplied by a factor of $1/\sqrt{2}$ can be taken as an approximation to the T_{10} interaction potential. The use of maps so obtained will be explained below.

In fact, for the purpose of symmetry considerations, the $\Delta U_s/\Delta q_i$ maps need not be calculated. The pattern of $\partial U_s/\partial q_i$ (see Figure 1) looks like a set of oppositely charged circles. On each atom, the line connecting their centers $\mathbf{C_i}$ is oriented along the direction of motion followed by that atom during a displacement of molecular geometry along the respective normal coordinate. Hence, the symmetry behavior of the T_{10} interaction potential can be visualized as

$$T_{10} \approx \sum_i^{3N} [s_i(+\mathbf{r}_i) + s_i(-\mathbf{r}_i)] \tag{6}$$

where s_i are charged spheres with a radius of $0.7Q_i$ centered at points $\mathbf{C_i} + 0.7\mathbf{Q_i}$ and $\mathbf{C_i} - 0.7\mathbf{Q_i}$. Hereafter, Q_i are normal coordinates normalized to unity (in au), whereas q_i are dimensionless normal coordinates. The adjustable parameter of 0.7 fits best to the $\partial U_s/\partial q_i$ maps of H_2 and CH_4. Comparison of the true and simulated $\partial U_s/\partial q_i$ maps in Figure 1 shows that simulated maps can be used as a simple tool for symmetry considerations. In this paper, however, we use $\partial U_s/\partial q_i$ maps calculated rigorously.

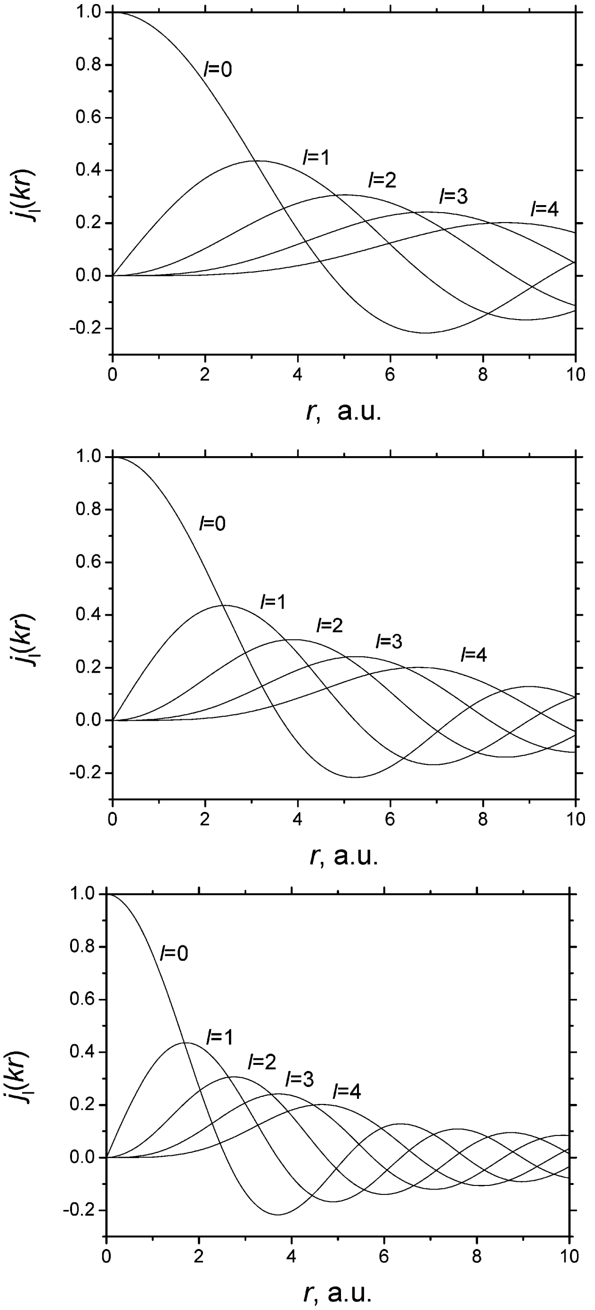

Figure 2. Spherical Bessel functions j_l for the electron energies of 6 (top), 10 (center), and 20 eV (bottom).

Assignment of symmetries to plane-wave functions requires their partial-wave expansion, used already in the very first attempts to explain angular distributions for the vibrational excitation of molecules by electron impact.[1,4] The formula for the partial-wave expansion is

$$e^{i\mathbf{k}\cdot\mathbf{r}} = 4\pi \sum_{l=0}^{\infty} \sum_{m=-l}^{m=l} i^l j_l(kr) Y^*_{lm}(\vartheta_r,\varphi_r) Y_{lm}(\vartheta_k,\varphi_k) \qquad (7)$$

For symmetry considerations, it is convenient to use real spherical harmonics defined as

$$Y^c_{l,m} = \frac{1}{\sqrt{2}}(Y_{l,m} + Y_{l,-m}) \quad \text{if } m = 0 \quad Y^c_{l0} = Y_{l0} \qquad (8)$$

$$Y^s_{l,m} = -i\frac{1}{\sqrt{2}}(Y_{l,m} - Y_{l,-m}) \quad \text{if } m = 0 \quad Y^s_{l0} = 0 \qquad (9)$$

TABLE 1: Real Spherical Functions

	symmetry				
	D_{4h}	T_d	Y_{lm} ($\theta = 0°$, $\varphi = 0°$)	Y_{lm} ($\theta = 90°$, $\varphi = 0°$)	Y_{lm} ($\theta = 180°$, $\varphi = 0°$)
Y_{00}	A_{1g}	A_1	0.2821	0.2821	0.2821
Y_{10}	A_{2u}	T_2	0.4886	0	−0.4886
Y^c_{11}	E_u	T_2	0	−0.4886	0
Y^s_{11}	E_u	T_2	0	0	0
Y_{20}	A_{1g}	E	0.6308	-0.3154	0.6308
Y^c_{21}	E_g	T_2	0	0	0
Y^s_{21}	E_g	T_2	0	0	0
Y^c_{22}	B_{1g}	E	0	0.5463	0
Y^s_{22}	B_{2g}	T_2	0	0	0
Y_{30}	A_{2u}	T_2	0.7464	0	−0.7464
Y^c_{31}	E_u	$T_1 + T_2$	0	0.4570	0
Y^s_{31}	E_u	$T_1 + T_2$	0	0	0
Y^c_{32}	B_{2u}	T_1	0	0	0
Y^s_{32}	B_{1u}	A_1	0	0	0
Y^c_{33}	E_u	$T_1 + T_2$	0	−0.5900	0
Y^s_{33}	E_u	$T_1 + T_2$	0	0	0

and to express the plane-wave function as

$$e^{i\mathbf{k}\cdot\mathbf{r}} = 4\pi \sum_{l=0}^{\infty} i^l j_l(kr) \sum_{m=0}^{m=l} [Y^c_{lm}(\vartheta_r,\varphi_r)Y^c_{lm}(\hat{\mathbf{k}}) + Y^s_{lm}(\vartheta_r,\varphi_r)Y^s_{lm}(\hat{\mathbf{k}})] \qquad (10)$$

Tables with symmetries of spherical harmonics Y_{l0}, Y^c_{lm}, and Y^s_{lm} can be found in the literature.[16] Hence, the integral $<k_2|T_{10}|k_1>$ is nonvanishing on symmetry grounds if the irreducible representation $\Gamma(q_i)$ is contained in the product $\Gamma(Y_{k2,l2m2}) \times \Gamma(Y_{k1,l1m1})$ of any pair of components of plane-waves $|k_2>$ and $|k_1>$. By means of partial-wave expansion of $|k_2>$ and $|k_1>$ plane-wave functions, we can express the T_{10} matrix element as follows

$$\langle k_2|T_{10}|k_1\rangle = \sum_{l2=0} \sum_{m2=0}^{l2} \sum_{l1=0} \sum_{m1=0}^{l1} [C^{cc}_{l2m2,l1m1}\, Y^c_{l2m2}(\hat{\mathbf{k}}_2)Y^c_{l1m1}(\hat{\mathbf{k}}_1) + C^{cs}_{l2m2,l1m1}\, Y^c_{l2m2}(\hat{\mathbf{k}}_2)Y^s_{l1m1}(\hat{\mathbf{k}}_1) + C^{sc}_{l2m2,l1m1}\, Y^s_{l2m2}(\hat{\mathbf{k}}_2)Y^c_{l1m1}(\hat{\mathbf{k}}_1) + C^{ss}_{l2m2,l1m1}\, Y^s_{l2m2}(\hat{\mathbf{k}}_2)Y^s_{l1m1}(\hat{\mathbf{k}}_1)] \qquad (11)$$

where the complex coefficients C are

$$C^{cc}_{l2m2,l1m1} = 16\pi^2 (i^{l2})^* i^{l1} \langle j_{l2}(k_2r)Y^c_{l2m2}(\vartheta_r,\varphi_r)|T_{10}|Y^c_{l1m1}(\vartheta_r,\varphi_r)j_{l1}(k_1r)\rangle \qquad (12)$$

$$C^{cs}_{l2m2,l1m1} = 16\pi^2 (i^{l2})^* i^{l1} \langle j_{l2}(k_2r)Y^c_{l2m2}(\vartheta_r,\varphi_r)|T_{10}|Y^s_{l1m1}(\vartheta_r,\varphi_r)j_{l1}(k_1r)\rangle \qquad (13)$$

$$C^{sc}_{l2m2,l1m1} = 16\pi^2 (i^{l2})^* i^{l1} \langle j_{l2}(k_2r)Y^s_{l2m2}(\vartheta_r,\varphi_r)|T_{10}|Y^c_{l1m1}(\vartheta_r,\varphi_r)j_{l1}(k_1r)\rangle \qquad (14)$$

$$C^{ss}_{l2m2,l1m1} = 16\pi^2 (i^{l2})^* i^{l1} \langle j_{l2}(k_2r)Y^s_{l2m2}(\vartheta_r,\varphi_r)|T_{10}|Y^s_{l1m1}(\vartheta_r,\varphi_r)j_{l1}(k_1r)\rangle \qquad (15)$$

Nonvanishing C coefficients are only those for which the product $Y_{l2m2}\cdot Y_{l1m1}$ has a component of the same symmetry as that of the vibrational coordinate q_i. We can also exclude additional C coefficients from the inspection of spherical Bessel functions j_l and the shapes of Y_{lm} functions. This will be done in the following paragraphs.

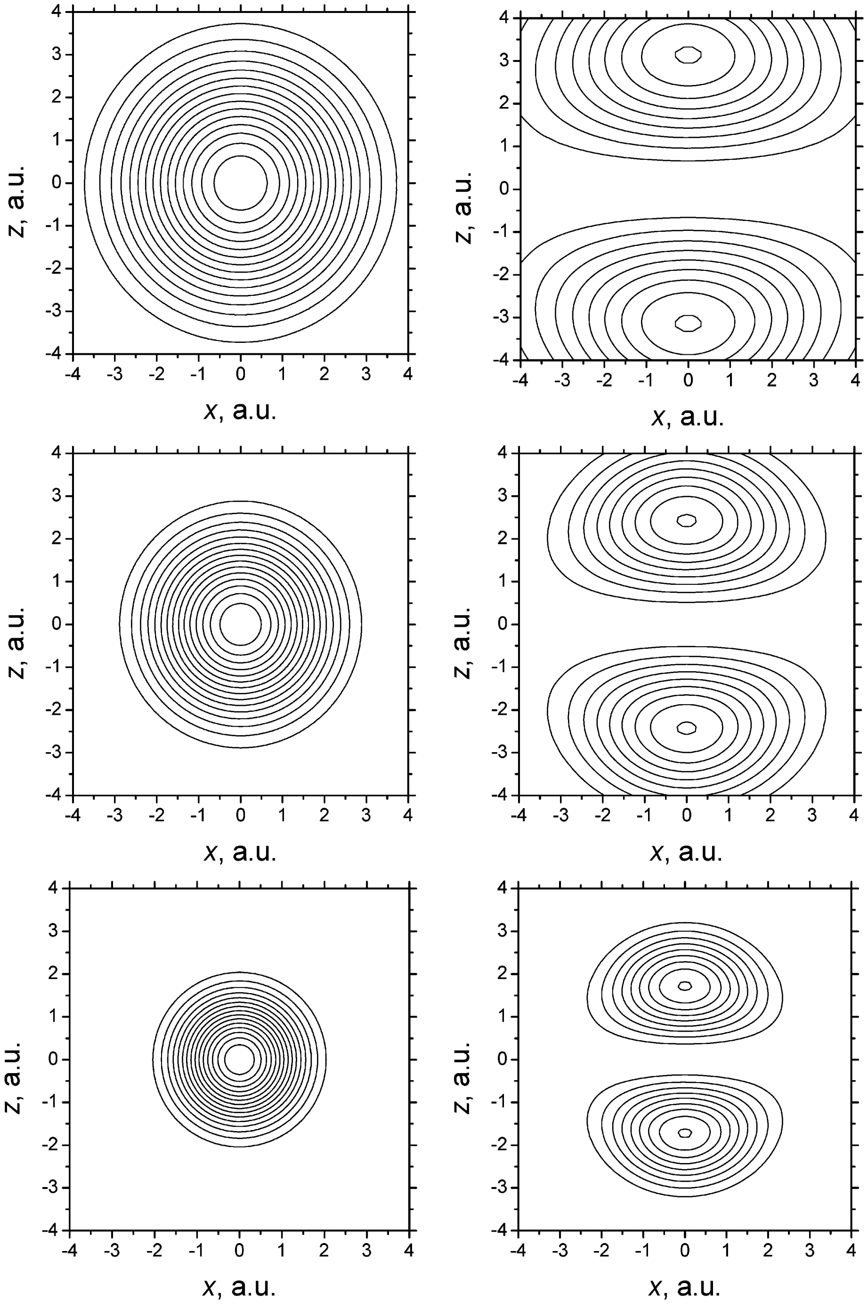

Figure 3. Maps of $j_0\cdot Y_{00}\cdot j_0\cdot Y_{00}$ (left) and $j_1\cdot Y_{10}\cdot j_1\cdot Y_{10}$ (right) for energies of 6 (top), 10 (center), and 20 eV (bottom). The maps are contoured with steps of 0.005. The contours with the highest values are at 0.075 (left) and 0.045 (right). The maps are invariant with respect to rotation around the *z* axis.

2.3. Spherical Bessel Functions. In Figure 2, we display spherical Bessel functions j_0−j_4 for electron energies of 6, 10, and 20 eV. As will be shown in the figures below, the derivative of the interaction potential $\partial U/\partial q_i$, and therefore also the T_{10} interaction potential, decay outside of the electronic cloud of the molecule. Hence, if the integral in eq 11 is to have a significant value, the Bessel functions j_{l1} and j_{l2} need to have an appreciable value just in the region where the electronic density is high. Figure 2 shows that this is satisfied only for the lowest values of *l*.

2.4. Shapes of Spherical Functions. Since the Y_{l2m2} functions in eqs 12−15 determine the direction of the outgoing electron (see $Y^{c}_{l2m2}(\hat{\mathbf{k}}_2)$ and $Y^{s}_{l2m2}(\hat{\mathbf{k}}_2)$ in eq 11), it is useful to recall the shapes of Y_{lm} functions. For example, if Y_{l2m2} is Y_{10}, Y_{20}, or Y_{30}, the favored direction for the outgoing electron is along the *z* axis. However, a nonzero value of a $C_{l2m2,l1m1}$ coefficient is not a sufficient condition for making this coefficient contribute. Also, the value of $Y_{l1m1}(\hat{\mathbf{k}}_1)$ in eq 11 for the incoming electron must be nonzero. The $C_{00,l1m1}$ coefficients contribute to isotropic scattering because the Y_{00} function (contributing to k_2) has no angular dependence. Because of the very anisotropic angular distribution observed in spatial dcs maps, we may assume that contributions from $C_{00,l1m1}$ will be small. The properties of real spherical functions Y^{c}_{lm} and Y^{s}_{lm} used in this paper are listed in Table 1.

2.5. Maps for Products of Spherical Functions. Values of coefficients *C* in eqs 12−15 can only be large if the symmetry of the product $j_{l2}\cdot Y_{l2m2}\cdot j_{l1}\cdot Y_{l1m1}$ conforms to the symmetry of T_{10}. This can be checked quickly by comparing the map of $j_{l2}\cdot Y_{l2m2}\cdot j_{l1}\cdot Y_{l1m1}$ with the map of T_{10}. As a substitute, the latter can be represented by the map of the derivative of the electrostatic potential, calculated or guessed from the geo-

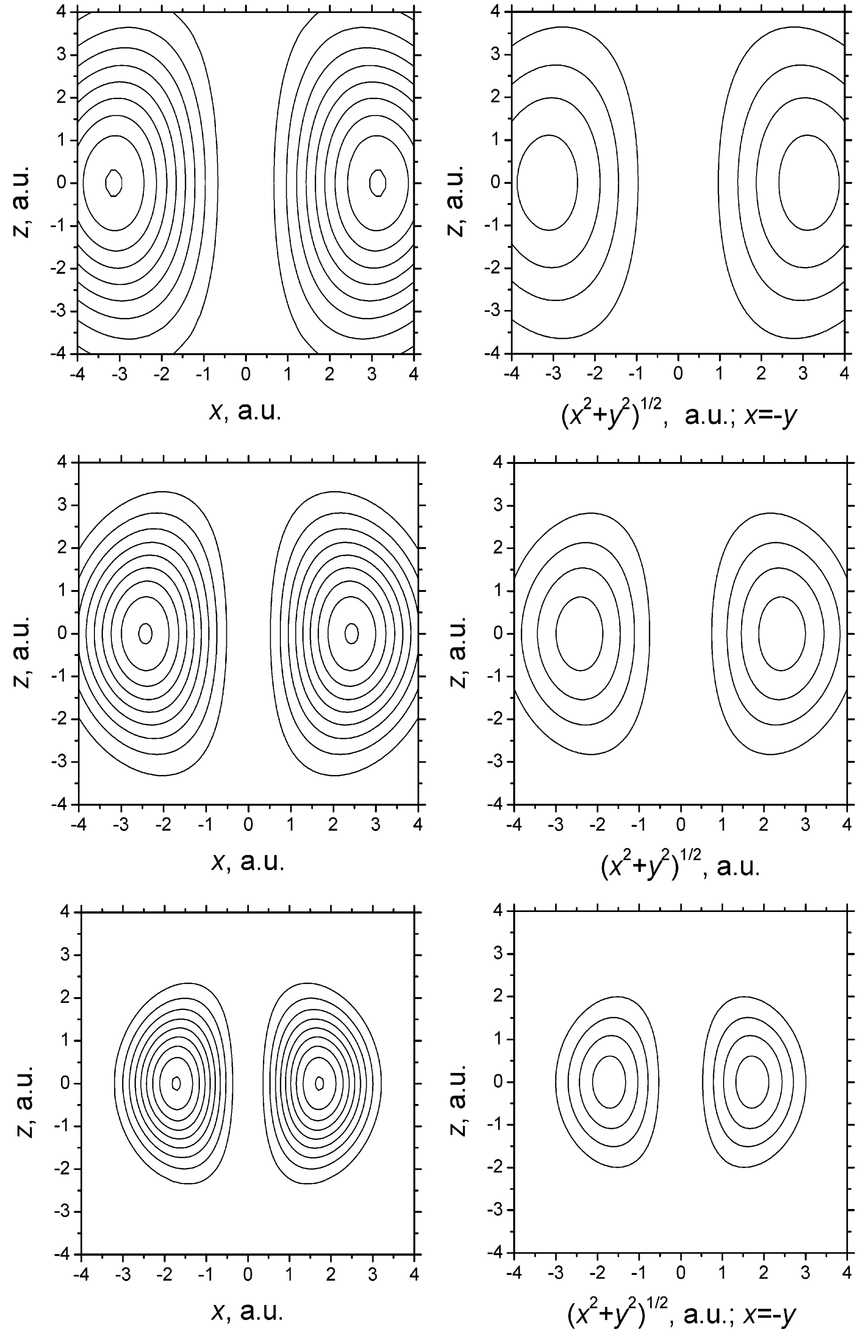

Figure 4. Maps of $j_1 \cdot Y^{c}_{11} \cdot j_1 \cdot Y^{c}_{11}$ for energies of 6 (top), 10 (center), and 20 eV (bottom). The maps are plotted in planes z versus x ($\varphi = 0°$, left) and H(2)−C−H(1) ($\varphi = -45°$, right). The same maps are obtained for $j_1 \cdot Y^{s}_{11} \cdot j_1 \cdot Y^{s}_{11}$ for energies of 6 (top), 10 (center), and 20 eV (bottom) when plotted in planes z versus y ($\varphi = 90°$, left) and H(2)−C−H(1) ($\varphi = -45$, right).

metrical representation of the normal mode alone, as noted above. The maps of $j_{l2} \cdot Y_{l2m2} \cdot j_{l1} \cdot Y_{l1m1}$ are general and can be precalculated and used for any molecular target. Contour graphs for products $j_{l2} \cdot Y_{l2m2} \cdot j_{l1} \cdot Y_{l1m1}$ with $l \leq 1$ are plotted in Figures 3−5. Some other relevant products are available in the Supporting Information (Figures S1−S18). Compared to the energy of the incoming electron (6, 10, or 20 eV), the vibrational excitation energy is small, and we can assume that $k_1 \approx k_2$. Therefore, the two $j_{l2}(kr)$ and $j_{l1}(kr)$ functions were evaluated for the same value of k.

2.6. Symmetry Considerations. As with the “allowed” transitions in photon spectroscopy, we require that the product $k_2 \cdot T_{10} \cdot k_1$ must contain a component which represents a totally symmetric integrand. It is therefore necessary to find a map of $j_{l2} \cdot Y_{l2m2} \cdot j_{l1} \cdot Y_{l1m1}$ which matches the $\partial U_s/\partial q_i$ map. In Figure 6, we present an example of an “allowed” and “forbidden” contribution. Obviously, in general, the situation is not as ideal as that in Figure 6, but at least with small symmetric molecules, a determination of allowed contributions is feasible.

In the next section, we will show the procedure for selecting the most relevant allowed contributions on the examples of H_2 and CH_4 molecules. We will proceed according to the following scheme. First, we will plot the $\partial U_s/\partial q_i$ maps as an approximation of the T_{10} maps. Then, we eliminate Y_{lm} functions for which the $Y_{lm}(\hat{\mathbf{k}}_1)$ values are zero. The success of this procedure depends on the selection of $j_{l2} \cdot Y_{l2m2} \cdot j_{l1} \cdot Y_{l1m1}$ maps that match the $\partial U_s/\partial q_i$ best. This permits us to truncate the expansion in eq 11 to a few terms and to predict the preferential angular distribution for a particular vibrational mode.

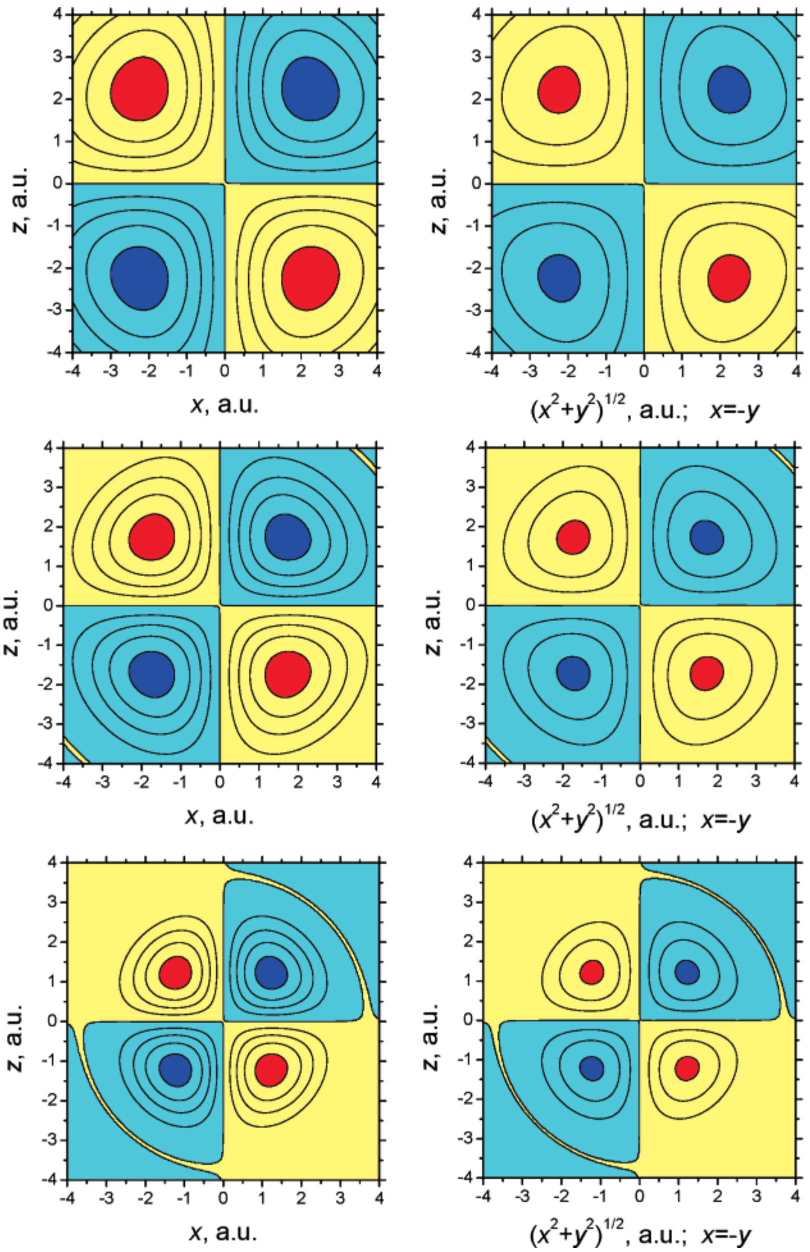

Figure 5. Maps of $j_1\cdot Y^c_{11}\cdot j_1\cdot Y_{10}$ for energies of 6 (top), 10 (center), and 20 eV bottom). The maps are plotted in planes z versus x ($\varphi = 0°$, left) and H(2)−C−H(1) ($\varphi = -45°$, right). Yellow and red mark regions of positive values, and blue regions are of negative values. The maps are contoured with steps of 0.005. The same maps are obtained for $j_1\cdot Y^s_{11}\cdot j_1\cdot Y_{10}$ when plotted in planes z versus y ($\varphi = 90°$, left) and that with $\varphi = -45°$ (right).

3. Spatial DCS Maps for the H_2 Molecule

In Figure 7, we present spatial dcs maps for incident electron energies of 6, 10, and 20 eV, obtained by rigorous solution of the Lippmann−Schwinger equation in the static exchange approximation (eqs 1−4).

3.1. Approximate T_{10} Map. We start the analysis of the angular distribution by plotting the derivative of the static potential, $\partial U_s/\partial q$, with respect to the normal coordinate. It may be assumed that the plot for T_{10} would have similar features. The shape of the plot (Figure 8) indicates which j_l and Y_{lm} functions in eqs 12−15 are optimal for high values of the coefficients $C_{l2m2,l1m1}$.

3.2. Selection of Bessel Functions. Figure 8 shows that the absolute value of $\partial U_s/\partial q$ is highest close to the positions of the nuclei. From Figure 2, it is seen that only the j_0, j_1, and j_2 functions have appreciable values in this region. Hence, the summation in eq 11 can be limited to $l \leq 2$.

3.3. Nonvanishing Y_{lm} Values for Fixed $\mathbf{k}_1$ Vectors. Consider separately the case of $\mathbf{k}_1$ parallel to the molecular axis z and $\mathbf{k}_1$ perpendicular to z. For the orientation $\mathbf{k}_1$ parallel to z, only Y_{00}, Y_{10}, and Y_{20} have nonzero values. In the case of $\mathbf{k}_1$ perpendicular to z in the σ_{xz} plane, the nonvanishing Y_{l1m1} functions with $l \leq 2$ in eq 11 are Y_{00}, Y^c_{11}, Y_{20}, and Y^c_{22}.

3.4. Truncated Expansion of $\langle k_2|\partial U/\partial q_i|k_1\rangle$ and Preferential Angular Distribution. Next, we examine which products of spherical functions have the same symmetry as the normal mode. For simplicity, we reduce the three-dimensional dcs map to a two-dimensional plot in the σ_{xz} plane, and we consider the D_{4h} point group. Hence, the product of the two spherical functions must also have a_{1g} symmetry. This condition is satisfied for $Y_{20}\cdot Y_{00}$ and all diagonal products $Y^c_{lm}\cdot Y^c_{lm}$ and $Y^s_{lm}\cdot Y^s_{lm}$. From Figures 3−5 and S1−S18 (in the Supporting Information), it is seen that plots for $Y_{10}\cdot Y_{10}$, followed by

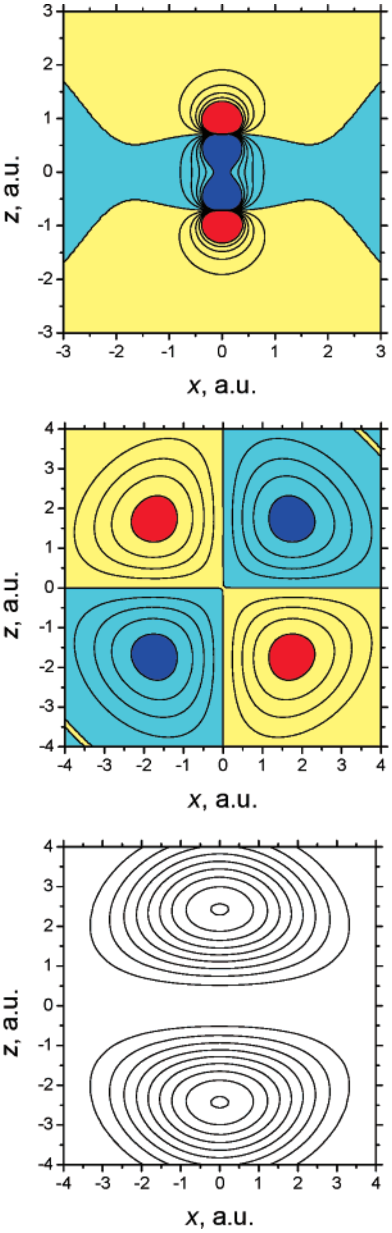

Figure 6. T_{10} map of H_2 approximated by the derivative of the electrostatic potential with respect to the vibrational stretching coordinate (top). The $j_1 \cdot Y^c_{11} \cdot j_1 \cdot Y_{10}$ map (center) does not match this map, and its contribution to the total amplitude vanishes. The $j_1 \cdot Y_{10} \cdot j_1 \cdot Y_{10}$ map (bottom) is oriented along the z axis similar to the T_{10} map, which suggests that the favored orientations of $\mathbf{k}_1$ and $\mathbf{k}_2$ are along the z axis (forward and backward scattering for $\mathbf{k}_1$ parallel to the z axis).

$Y_{00} \cdot Y_{00}$ and $Y_{20} \cdot Y_{20}$, match the map of $\partial U_s/\partial q$ best. Consider therefore the amplitude in the following form

$$\langle k_2|T_{10}|k_1\rangle \approx C^{cc}_{00,00} Y_{00}(\hat{\mathbf{k}}_2) Y_{00}(\hat{\mathbf{k}}_1) + C^{cc}_{20,20} Y_{20}(\hat{\mathbf{k}}_2) Y_{20}(\hat{\mathbf{k}}_1) + C^{cc}_{10,10} Y_{10}(\hat{\mathbf{k}}_2) Y_{10}(\hat{\mathbf{k}}_1) \quad (16)$$

All three products have the right symmetry. Some products of Y^c_{11}, Y^s_{11}, and also Y_{30}, Y^c_{31}, Y^s_{31}, Y^c_{33}, and Y^s_{33} can conform by symmetry, but their contributions will be small because of the size mismatch. $C_{00,00}$ and $C_{00,20}$ represent the Y_{00} isotropic contribution to k_2 and can be therefore expected to be small. Compared to the energy of the incoming electron (6, 10, or 20 eV), the vibrational excitation energy is small, and we can assume that $k_1 \approx k_2$ and, consequently, $C_{20,00} \approx C_{00,20}$ and, in general, $C_{l2m2,l1m1} \approx C_{l1m1,l2m2}$.

Consider first the case of $\mathbf{k}_1$ parallel to the molecular axis z. For this orientation, only Y_{00}, Y_{10}, and Y_{20} have nonzero values. $Y_{10}(\hat{\mathbf{k}}_2)$ and $Y_{20}(\hat{\mathbf{k}}_2)$ orient $\mathbf{k}_2$ along the z axis, though Y_{20} has also a small lobe perpendicular to z. Nevertheless, we can expect that the shape of the plot in the spatial dcs map is determined by the $C_{10,10}$ contribution. Next, we calculate the weights of contributions by evaluation of spherical harmonics (from Table 1) in eq 16. Weights of $Y(\hat{\mathbf{k}}_2) \cdot Y(\hat{\mathbf{k}}_1)$ favor the location of $\mathbf{k}_2$ in the $+z$ and $-z$ directions. Notice that the graphs for 6, 10, and 20 eV in Figure 7 are not plotted on the same scale. As the energy of the scattering electron is increased, the overlap of $j_1 \cdot Y_{10} \cdot j_1 \cdot Y_{10}$ with $\partial U_s/\partial q$ drops, and the differential cross section decreases. For $\mathbf{k}_2$ ($\theta = 90°$) perpendicular to $\mathbf{k}_1$ ($\theta = 0°$), we have $Y_{10}(\hat{\mathbf{k}}_2) = 0$, and the main contribution given by $C_{10,10}$ vanishes. $C_{20,00}$ and $C_{20,20}$ contributions are again small because Y_{20} is primarily oriented along the z axis and has only a small lobe perpendicular to the z direction. Also, $C_{00,20}$ is small because $C_{20,00} \approx C_{00,20}$, as already noted. Moreover, the two contributions tend to cancel because $Y_{20}(\hat{\mathbf{k}}_2) \cdot Y_{00}(\hat{\mathbf{k}}_1) = -0.0890$ and $Y_{00}(\hat{\mathbf{k}}_2) \cdot Y_{20}(\hat{\mathbf{k}}_1) = 0.1779$. Compared to the forward and backward scattering, the scattering perpendicular to the molecular axis can be expected to be small, and this agrees with the calculated spatial dcs maps (Figure 7).

In the case of $\mathbf{k}_1$ perpendicular to the molecular axis z in the σ_{xz} plane, the nonvanishing Y_{l1m1} functions with $l \leq 2$ in eq 11 are Y_{00}, Y^c_{11}, Y_{20}, and Y^c_{22}. The map for $Y^c_{22} \cdot Y^c_{22}$ in Figure S11 indicates that this contribution can be disregarded. It may be assumed that the amplitude can be approximated as

$$\langle k_2|T_{10}|k_1\rangle \approx C_{00,00} Y_{00}(\hat{\mathbf{k}}_2) Y_{00}(\hat{\mathbf{k}}_1) + C^{cc}_{11,11}\, Y^c_{11}(\hat{\mathbf{k}}_2) Y^c_{11}(\hat{\mathbf{k}}_1) + C_{20,20} Y_{20}(\hat{\mathbf{k}}_2) Y_{20}(\hat{\mathbf{k}}_1) \quad (17)$$

All three terms in eq 17 give rise only to weak scattering oriented along the x axis, in accordance with the spatial dcs map in Figure 7. Preference for forward over backward scattering is due to a partial cancellation of the three terms in eq 17, but this cannot be determined from symmetry alone.

4. Spatial DCS Maps for the CH_4 Molecule

With the methane molecule, two normal modes are IR active and two are IR inactive. According to the spectroscopic convention, the symmetric stretch is designated as ν_1. It is of a_1 symmetry, and the normal coordinate is

$$Q_1 = 1/2(r_1 + r_2 + r_3 + r_4) \quad (18)$$

The bending mode of e symmetry is designated as ν_2, and the normal coordinate is

$$Q_{2a} = (1/\sqrt{12})(2\alpha_{12} - \alpha_{13} - \alpha_{23} + 2\alpha_{34} - \alpha_{14} - \alpha_{24}) \quad (19a)$$

$$Q_{2b} = 1/2(\alpha_{23} - \alpha_{13} + \alpha_{14} - \alpha_{24}) \quad (19b)$$

The meaning of indices 1−4 is defined in Figure 9. The spatial dcs maps for coordinates Q_1 and Q_{2a} and electron energies of 6, 10, and 20 eV are presented in Figure 10 for $\mathbf{k}_1$ oriented along the direction of the C−H(1) bond and in Figures 11 and 12 for the positive direction along the z axis. The $\mathbf{k}_2$ vector is chosen to lie in the planes defined by atoms H(1), C, and H(2) ($\varphi_2 = 135°$) and H(3), C, and H(4) ($\varphi_2 = 45°$).

4.1. Approximate T_{10} Maps. We start the analysis of the angular distribution by inspection of the maps of the derivative of the static potential, $\partial U_s/\partial q$, with respect to normal coordinates. Figure 13 shows that the derivative is highest close to positions

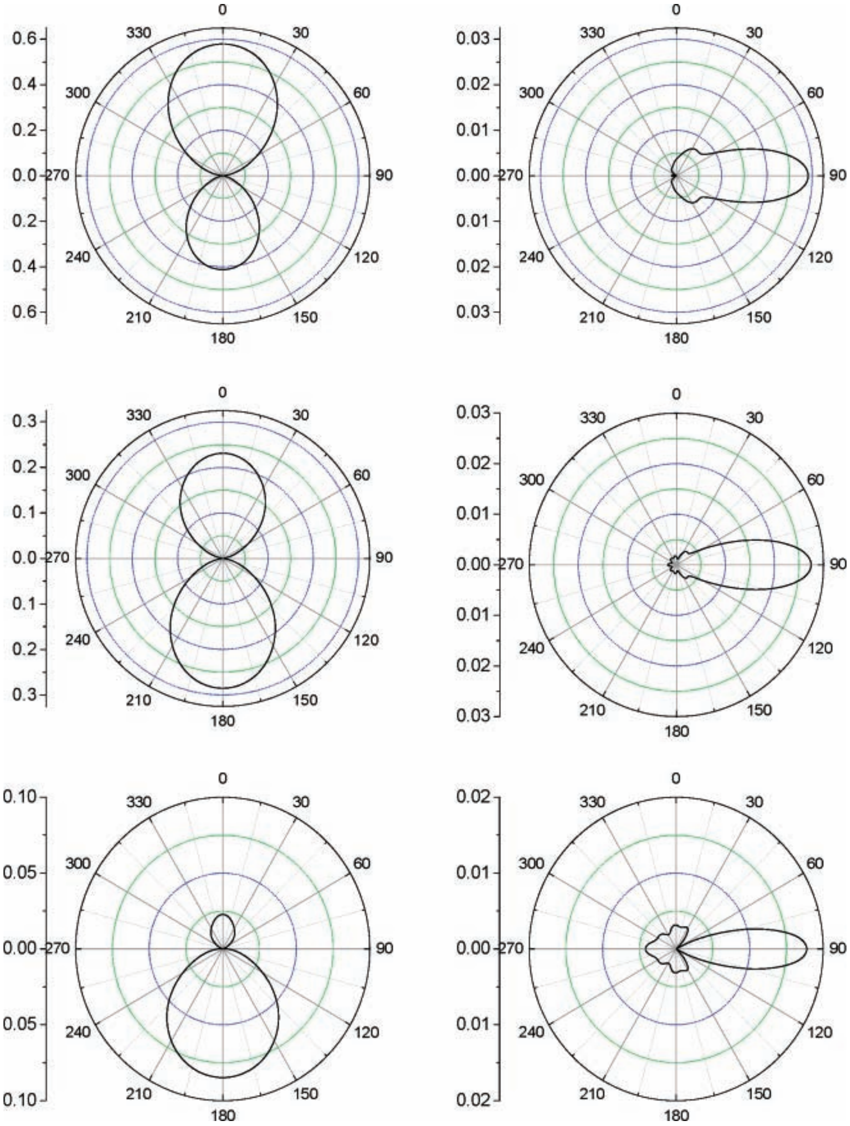

Figure 7. Spatial dcs maps for the H_2 molecule for the incident electron energy of 6 (top), 10 (center), and 20 eV (bottom). The $\mathbf{k}_1$ vector is parallel (left) or perpendicular (right) to the principal molecular axis. Note that maps are plotted on different scales. The H_2 molecule is oriented along the axis 0−180°.

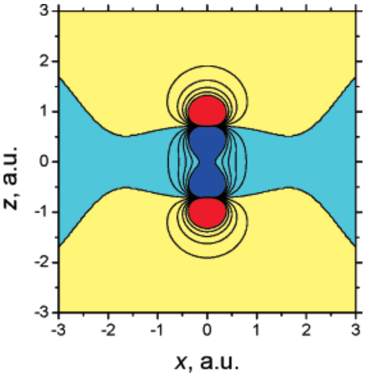

Figure 8. Map of the derivative of the electrostatic potential of H_2 with respect to the normal coordinate in the σ_{xz} plane. Nuclei are positioned at $z = \pm 0.715$ au. The map is contoured with a step of 0.1

of hydrogen atoms, that is, about 2 au from the origin of the coordinate system along the C−H bonds, and that it can be taken as vanishingly small for $r > 4$ au.

4.2. Selection of Bessel Functions. In contrast to the hydrogen molecule, plots of Bessel functions in Figure 2 indicate that in addition to j_0, j_1, and j_2, the function j_3 may also have

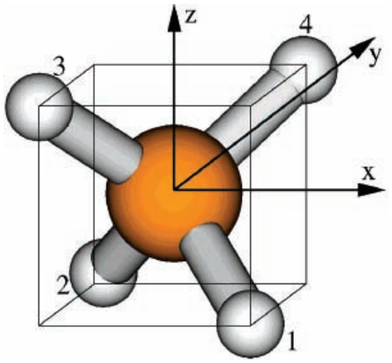

Figure 9. Tetrahedral structure of CH_4 in the coordinate system.

appreciable values in the region where the derivative of the static potential is large. The limitation to $l \leq 2$ in eqs 12−15 is only justified for 6 and 10 eV.

4.3. Nonvanishing Y_{lm} Values for the Fixed $\mathbf{k}_1$ Vectors. If we choose $\mathbf{k}_1$ to be oriented along the CH(1) bond ($\theta = 125$ and $\varphi = -45°$), Y_{20}, Y_{22}^{c}, and Y_{32}^{c} have zero $Y(\hat{\mathbf{k}}_1)$ values and can be dropped from further consideration. If we choose $\mathbf{k}_1$ to

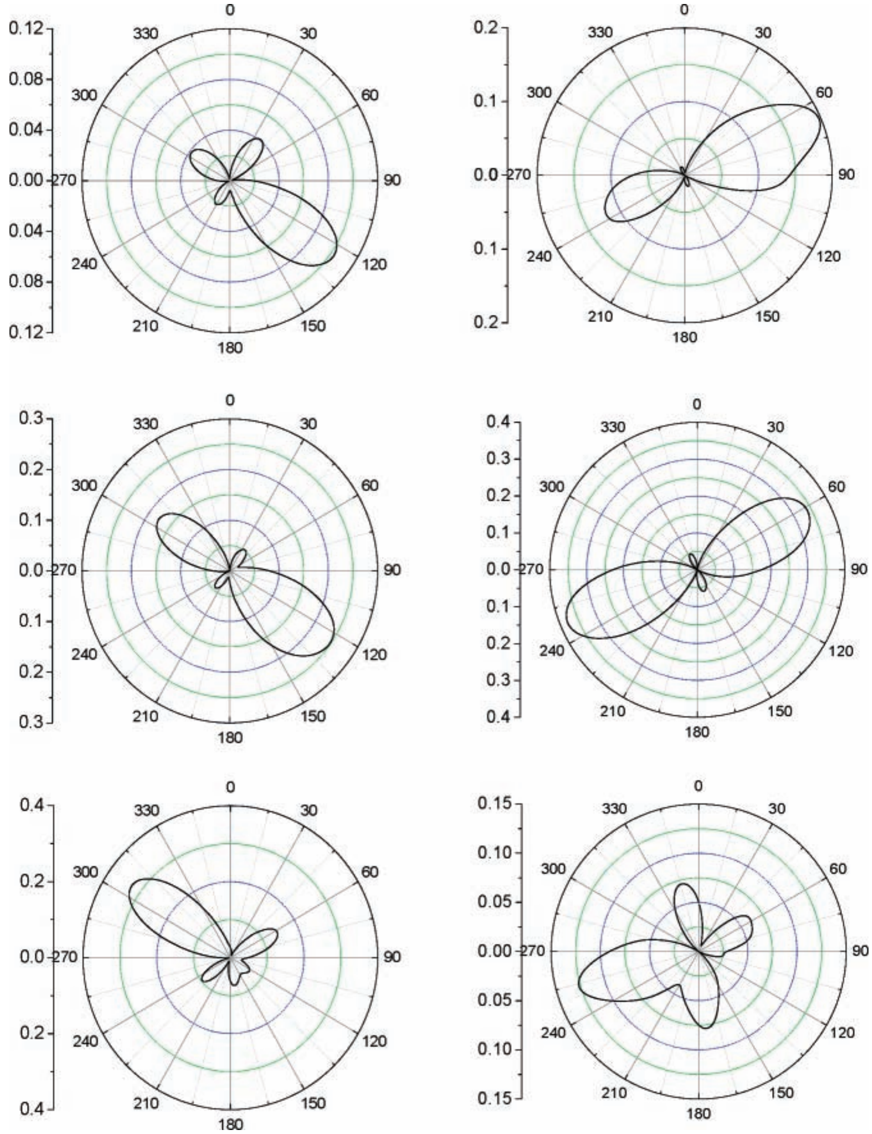

Figure 10. Spatial dcs maps for the symmetric CH stretch (left) and the bending e mode (right) in CH_4 and incident electron energies of 6 (top), 10 (center), and 20 eV (bottom). The $\mathbf{k}_1$ vector is parallel to the CH(1) bond ($\theta = 125°$), and $\mathbf{k}_2$ lies in the H(2)−C−H(1) plane.

be oriented along the *z* axis, the only nonzero $Y(\hat{\mathbf{k}}_1)$ values are Y_{00}, Y_{10}, Y_{20}, and Y_{30}.

4.4. Truncated Expansion of $<k_2|\partial U/\partial q_i|k_1>$ and Preferential Angular Distribution. The symmetry of the symmetric stretching mode ν_1 is a_1, which means that allowed pairs of spherical functions in eq 11 must be of $A_1 \times A_1$, $E \times E$, $T_1 \times T_1$, or $T_2 \times T_2$ symmetry. We determine next, by inspection of Figures 3−5 and S1−S18 in the Supporting Information, which pair of contributions $j_{l2}{\cdot}Y_{l2m2}{\cdot}j_{l1}{\cdot}Y_{l1m1}$ conform to the $\partial U_s/\partial q_1$ maps best. This is straightforward for energies of 6 and 10 eV. As noted above, we can limit ourselves to $l \leq 2$ in this case, and we find that the optimum fit is provided by the $j_2{\cdot}Y^c_{21}{\cdot}j_2{\cdot}Y^c_{21}$, $j_2{\cdot}Y^s_{21}{\cdot}j_2{\cdot}Y^s_{21}$, and $j_2{\cdot}Y^s_{22}{\cdot}j_2{\cdot}Y^s_{22}$ terms (Figures S5 and S11). Note that $j_2{\cdot}Y^s_{22}{\cdot}j_2{\cdot}Y^s_{22}$ conforms to the $\partial U_s/\partial q$ map at positions of all four hydrogen atoms, whereas $j_1{\cdot}Y^s_{11}{\cdot}j_1{\cdot}Y^c_{11}$ or $j_2{\cdot}Y^s_{21}{\cdot}j_1{\cdot}Y^c_{11}$, for example, do not. This reduces eq 11 to

$$\langle k_2|T_{10}|k_1\rangle \approx C^{cc}_{21,21}\, Y^c_{21}(\hat{\mathbf{k}}_2)Y^c_{21}(\hat{\mathbf{k}}_1) + C^{ss}_{21,21}\, Y^s_{21}(\hat{\mathbf{k}}_2)Y^s_{21}(\hat{\mathbf{k}}_1) + C^{ss}_{22,22}\, Y^s_{22}(\hat{\mathbf{k}}_2)Y^s_{22}(\hat{\mathbf{k}}_1) \quad (20)$$

If we choose $\mathbf{k}_1$ to be oriented along the CH(1) bond and $\mathbf{k}_2$ to lie in the H(2)−C−H(1) plane, all three products $Y^c_{21}(\hat{\mathbf{k}}_2)Y^c_{21}(\hat{\mathbf{k}}_1)$, $Y^s_{21}(\hat{\mathbf{k}}_2)Y^s_{21}(\hat{\mathbf{k}}_1)$, and $Y^s_{22}(\hat{\mathbf{k}}_2)Y^s_{22}(\hat{\mathbf{k}}_1)$ are zero for $\theta = 0$, 90, 180, and 270°. Their sum is $\pm 0.363 \times 0.364$ for $\theta = 55$, 235, and 305° and $3 \times 0.363 \times 0.364$ for $\theta = 125°$. This is in qualitative agreement with the spatial dcs maps presented in Figure 10. When the energy of the incident electron is 20 eV, the situation is more complicated. The highest values of $\partial U_s/\partial q_1$ are localized at the positions of the hydrogen atoms (corners of the *xyz* cube; see Figure 13). As Figure 2 shows, at *r* equal to the CH bond length (2.25 au), the Bessel function $j_3(kr)$ also has to be taken into account. Actually, $j_3{\cdot}Y^s_{32}{\cdot}j_3{\cdot}Y^s_{32}$ (Figure S18) gives the largest contribution and must be added to the three terms in eq 20. Also, the product $Y^s_{32}(\hat{\mathbf{k}}_2)Y^s_{32}(\hat{\mathbf{k}}_1)$ is zero for $\theta = 0$, 90, 180, and 270°, which explains why the map for 20 eV in Figure 10 does not show any contribution at these scattering angles. However, the observed preference of backward scattering over the forward scattering cannot be explained by this simple approach. Some conclusions can be drawn from eq 20 itself. If we also add $Y^s_{32}(\hat{\mathbf{k}}_2)Y^s_{32}(\hat{\mathbf{k}}_1)$ to the right-hand side of eq 20, k_2 is represented by a combination of $Y^c_{21}(\hat{\mathbf{k}}_2)$, $Y^s_{21}(\hat{\mathrm{k}})_2$, $Y^s_{22}(\hat{\mathbf{k}}_2)$, and $Y^s_{32}(\hat{\mathbf{k}}_2)$, that is, by *xz*-, *yz*-, *yx*-, and *xyz*-type functions. This means that preferential directions for the

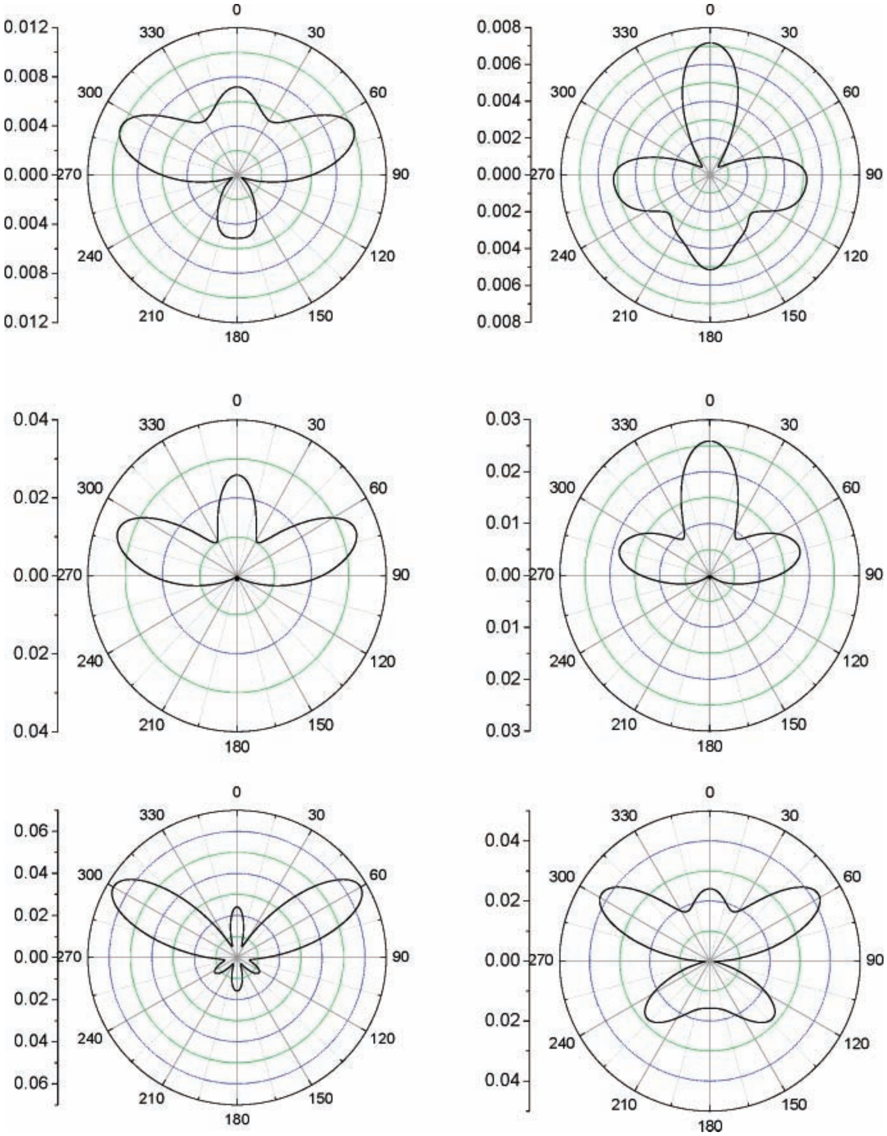

Figure 11. Spatial dcs maps for the symmetric CH stretch in CH_4 and incident electron energies of 6 (top), 10 (center), and 20 eV (bottom). The $\mathbf{k}_1$ vector is parallel to the z axis, and $\mathbf{k}_2$ lies in the H(2)−C−H(1) (left) and H(3)−C−H(4) (right) planes.

outgoing electron are along the C−H bonds, not along directions bisecting the valence angles H−C−H.

If we choose $\mathbf{k}_1$ to be oriented along the z axis, the situation is different. Now, Y_{00}, Y_{10}, Y_{20}, and Y_{30} are the only $Y(\hat{\mathbf{k}}_1)$ functions that are significant. This excludes the four main contributions $Y^{c}_{21}(\hat{\mathbf{k}}_2)Y^{c}_{21}(\hat{\mathbf{k}}_1)$, $Y^{s}_{21}(\hat{\mathbf{k}}_2)Y^{s}_{21}(\hat{\mathbf{k}}_1)$, $Y^{s}_{22}(\hat{\mathbf{k}}_2)Y^{s}_{22}(\hat{\mathbf{k}}_1)$, and $Y^{s}_{32}(\hat{\mathbf{k}}_2)Y^{2}_{32}(\hat{\mathbf{k}}_1)$ noted above. Scattering is therefore much weaker (Figure 11) than it was when the incident electron approached the molecule along the C−H(1) bond. The only symmetry-allowed contributions $Y^{c,s}_{l2,m2}\cdot Y_{l1,0}$ are $Y_{00}\cdot Y_{00}$ ($A_1 \times A_1$), $Y_{20}\cdot Y_{20}$ (E × E), and all contributions $Y^{c,s}_{l2,m2}\cdot Y_{10}$ and $Y^{c,s}_{l2,m2}\cdot Y_{30}$ of the $T_2 \times T_2$ symmetry (See Table 1). Again, the inspection of Figures 3−5 and S1−S18 can reduce this list. As a matter of fact, no ideal fit to $\partial U_s/\partial q_1$ is found. $Y^{s}_{32}(\hat{\mathbf{k}}_2)Y_{00}(\hat{\mathbf{k}}_1)$ (Figure S16) seems to conform best, followed by $Y_{10}(\hat{\mathbf{k}}_2)Y_{10}(\hat{\mathbf{k}}_1)$ (Figure 3) and $Y_{30}(\hat{\mathbf{k}}_2)Y^{s}_{22}(\hat{\mathbf{k}}_1)$ (Figure S14), and to a lesser extent to $Y_{20}(\hat{\mathbf{k}}_2)Y_{20}(\hat{\mathbf{k}}_1)$ (Figure S2). Hence, we express eq 11 in the form

$$\langle k_2|T_{10}|k_1\rangle \approx C^{sc}_{32,00}\, Y^{s}_{32}(\hat{\mathbf{k}}_2)Y_{00}(\hat{\mathbf{k}}_1) + C_{10,10}Y_{10}(\hat{\mathbf{k}}_2)Y_{10}(\hat{\mathbf{k}}_1) + C^{s}_{22,30}\, Y^{s}_{22}(\hat{\mathbf{k}}_2)Y_{30}(\hat{\mathbf{k}}_1) + C_{20,20}Y_{20}(\hat{\mathbf{k}}_2)Y_{20}(\hat{\mathbf{k}}_1) \quad (21)$$

and assume accordingly that the plane-wave function k_2 can be represented as a linear combination of Y^{s}_{32}, Y_{10}, Y^{s}_{22}, and Y_{20}. Y_{10} and Y_{20} are z and z^2 functions, respectively, and they direct the outgoing electron along the z axis (forward and backward). Y^{s}_{32} and Y^{s}_{22} are xyz- and xy-type functions, respectively, and together, they orient the outgoing electron into the “wings” of plots in Figure 11. If those maps are plotted as z versus x and z versus y plots, the maps lose their “wings”, and only forward and backward scattering is observed because Y^{s}_{32} and Y^{s}_{22} are zero in these planes. In contrast to the preceding case of $\mathbf{k}_1$ parallel to the C−H(1) bond, the outgoing electron avoids the hydrogen atoms.

Consider now the bending mode ν_2. Its symmetry is e, which means that allowed pairs of spherical functions in eq 11 must be of $A_1 \times E$, $T_1 \times T_1$, $T_1 \times T_2$, or $T_2 \times T_2$ symmetry. The list of allowed terms can be reduced by inspection of Figures 3−5 and S1−S18, which suggest that for low energies (6 and 10 eV), the best fit for the $\partial U_s/\partial q_2$ map (Figure 13) is provided by $Y^{s}_{22}\cdot Y^{s}_{22}$, $Y^{c}_{21}\cdot Y^{c}_{21}$, $Y^{s}_{21}\cdot Y^{s}_{21}$, and to a lesser extent by $Y^{s}_{22}\cdot Y_{10}$ and $Y_{10}\cdot Y^{s}_{22}$ terms. This means that, as with the symmetric stretch, the T_{10} element can be approximated by eq 20. We limit

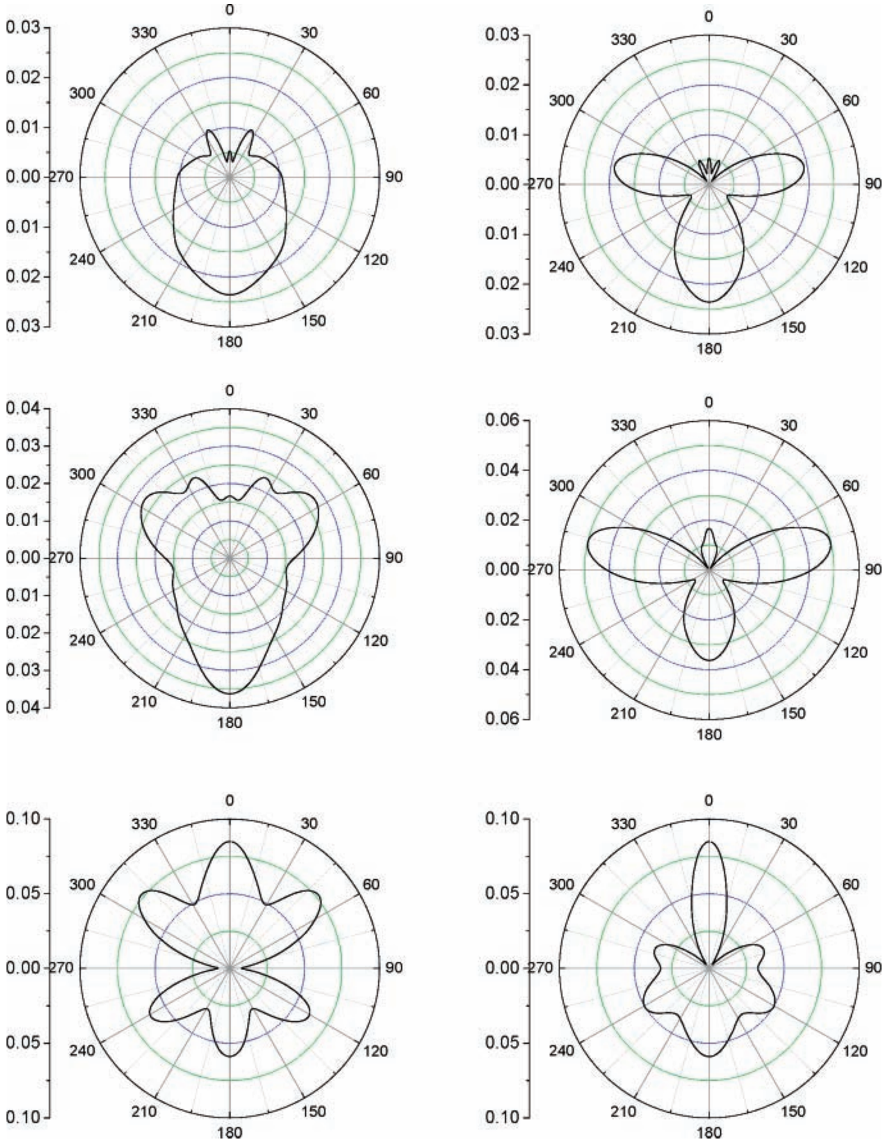

Figure 12. Spatial dcs maps for the e bending mode of CH_4 and incident electron energies of 6 (top), 10 (center), and 20 eV (bottom). The $\mathbf{k}_1$ vector is parallel to the *z* axis, and $\mathbf{k}_2$ lies in the H(2)−C−H(1) (left) and H(3)−C−H(4) (right) planes. Note that the maps are on different scales.

ourselves to the case of $\mathbf{k}_2$ lying in the H(2)−C−H(1) plane. Figure S11 shows that the $j_2{\cdot}Y^{s}_{22}.j_2{\cdot}Y^{s}_{22}$ density is higher in the region where $\partial U_s/\partial q_2$ is negative than in the region where $\partial U_s/\partial q_2$ is positive (Figure 13). In contrast, $j_2{\cdot}Y^{c}_{21}{\cdot}j_2{\cdot}Y^{c}_{21}$ and $j_2{\cdot}Y^{s}_{21}{\cdot}j_2{\cdot}Y^{s}_{21}$ densities (Figure S5) are higher in the region where $\partial U_s/\partial q_2$ is positive than they are in the region where $\partial U_s/\partial q_2$ is negative. Therefore, we may conclude that $C^{ss}_{22,22}$ is of the opposite sign than $C^{cc}_{21,21}$ and $C^{ss}_{21,21}$. From eqs 13 and 14, it may be concluded (from the imaginary factor) that $C^{cs}_{10,22} \approx -C^{sc}_{22,10}$. Consider two orientations of $\mathbf{k}_1$. For $\mathbf{k}_1$ parallel to the CH(1) bond, $Y_{10}(\hat{\mathbf{k}}_1) = -0.282$, $Y^{c}_{21}(\hat{\mathbf{k}}_1) = 0.364$, $Y^{s}_{21}(\hat{\mathbf{k}}_1) = -0.364$, and $Y^{s}_{22}(\hat{\mathbf{k}}_1) = -0.364$. This permits us to estimate relative ratios of differential cross sections for four preferential directions of $\mathbf{k}_2$. For forward scattering ($\theta = 125°$), $Y^{s}_{22}(\hat{\mathbf{k}}_2)Y_{10}(\hat{\mathbf{k}}_1) = (-0.364) \times (-0.282) = 0.103$ and $Y_{10}(\hat{\mathbf{k}}_2)Y^{s}_{22}(\hat{\mathbf{k}}_1) = (-0.282) \times (-0.364) = 0.103$. Thus, the two contributions tend to cancel (because $C^{cs}_{10,22} \approx -C^{sc}_{22,10}$, as noted above). Also $Y^{c}_{21}Y^{c}_{21}$ and $Y^{s}_{21}Y^{s}_{21}$ tend to cancel the $Y^{s}_{22}Y^{s}_{22}$ contribution because $Y^{c}_{21}(\hat{\mathbf{k}}_2)Y^{c}_{21}(\hat{\mathbf{k}}_1) = 0.364 \times 0.364 = 0.135$, $Y^{s}_{21}(\hat{\mathbf{k}}_2)Y^{s}_{21}(\hat{\mathbf{k}}_1) = (-0.364) \times (-0.364) = 0.135$, and $Y^{s}_{22}(\hat{\mathbf{k}}_2)Y^{s}_{22}(\hat{\mathbf{k}}_1) = (-0.364) \times (-0.364) = 0.135$. This partial cancellation occurs because the sign of $C^{ss}_{22,22}$ is opposite of those of $C^{cc}_{21,21}$ and $C^{ss}_{21,21}$. The same cancellation occurs with backward scattering. In contrast, at $\theta = 55$ and 235°, the three contributions are of the same sign, giving rise to two lobes observed in spatial dcs maps (Figure 10). For the energy of 20 eV, the situation is more complicated. For this energy, the Bessel function j_3 (Figure 2) has an appreciable value in the region of high $\partial U_s/\partial q_2$ density (Figure 13), and contributions with $l = 3$ cannot be excluded a priori. Actually, Figure S13 shows that the term $j_3{\cdot}Y^{s}_{32}{\cdot}j_2{\cdot}Y_{20}$ conforms ideally to the $\partial U_s/\partial q_2$ density, and therefore, it also should be taken into account. Assuming $\mathbf{k}_1$ to be parallel to the CH(1) bond, $Y_{20}(\hat{\mathbf{k}}_1) = 0.000$ and $Y^{s}_{32}(\hat{\mathbf{k}}_1) = 0.556$. Hence, we are only left with the $Y_{20}(\hat{\mathbf{k}}_2)Y^{s}_{32}(\hat{\mathbf{k}}_1)$ term. Its value is largest in the $+z$ and $-z$ directions, giving rise to two additional lobes in the spatial dcs map for this energy (Figure 10).

If $\mathbf{k}_1$ is parallel to the *z* axis, the nonvanishing components of k_1 are only Y_{00}, Y_{10}, Y_{20}, and Y_{30}, and the main terms from the last paragraph, $Y^{s}_{22}{\cdot}Y^{s}_{22}$, $Y^{c}_{21}{\cdot}Y^{c}_{21}$, and $Y^{s}_{21}{\cdot}Y^{s}_{21}$, cannot contribute. Differential cross sections for this orientation of $\mathbf{k}_1$ are therefore considerably smaller (compare scales of Figures 10

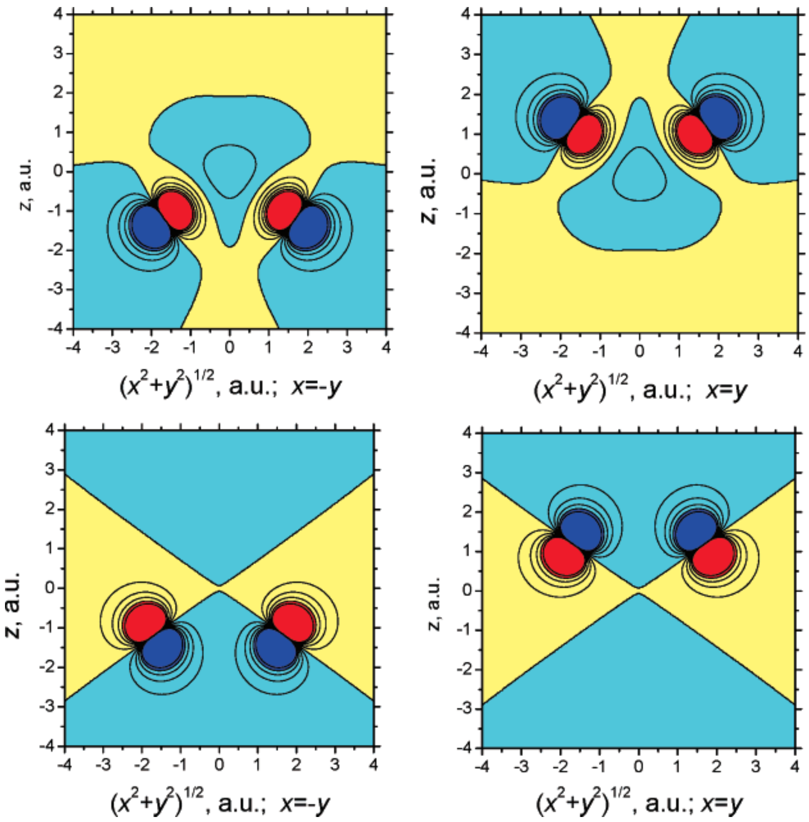

Figure 13. Maps of the derivative of the electrostatic potential of CH_4 with respect to the symmetric stretching (top) and bending 2a (bottom) normal coordinates. The plots are in the H(2)−C−H(1) (left) and H(3)−C−H(4) (right) planes, and the center of mass is at $z = 0$. The step in contours is 0.1.

and 12) and do not show much anisotropy. The difference of the spatial dcs maps for the energy of 20 eV from those for 6 and 10 eV can be explained by the contribution of terms with $l = 3$. A distinct contribution is due to the $j_3 \cdot Y_{30} \cdot j_3 \cdot Y_{30}$ term (Figure S13), which gives rise to forward scattering.

5. Conclusions

We have found that it is possible to understand the results of ab initio computations of the angular distribution of vibrationally inelastic nonresonant scattering qualitatively in relatively simple terms. If the form of the vibrational normal modes is known, this can actually be done without recourse to a computer. The procedure is as follows: (1) guess the $\partial U/\partial q_i$ map from the geometrical representation of the normal mode alone, as explained in section 2.2; (2) inspect Bessel functions in Figure 2 and select those that have appreciable value in the range of high values of $\Delta U_s/\Delta q_i$; (3) fix the $\mathbf{k}_1$ vector and determine the nonvanishing Y_{lm} values for this orientation; (4) set up a truncated expansion of the $<k_2|\partial U/\partial q_i|k_1>$ element, as shown by eq 11; (5) inspect the contributions to the plane-wave function k_2 and, with help of their weights ($Y_{l2m2} \cdot Y_{l1m1}$ in eq 11), determine the preferential directions for the scattered electron. If desired, instead of guessing the $\partial U/\partial q_i$ map, as described in section 2.2, it is possible to obtain it in a somewhat more laborious but also more reliable way by means of commonly accessible quantum chemical software. For the selected ith vibrational mode of the target, electrostatic potential maps can be calculated at the geometries distorted from the equilibrium geometry along the vibrational coordinate q_i by $+\Delta q_i$ and $-\Delta q_i$. By numerical differentiation, the $\Delta U_s/\Delta q_i$ map is obtained.

We illustrate the procedure on the examples of H_2 and CH_4 molecules. In both cases, the qualitatively deduced angular distribution agrees with the calculated spatial dcs maps. It has not been our primary objective to develop an approximate method of calculation of vibrationally inelastic vibrational cross sections but, rather, to obtain intuitive understanding of the results of the ab initio method. Still, it is conceivable that the simple procedure could be used to make qualitative predictions for larger molecules, including those for which a full ab initio treatment may be presently prohibitively expensive. It is unclear whether the number of required Bessel functions (Figure 2) would then not become excessive, even for localized vibrations, and we intend to examine these issues next.

Acknowledgment. This work was supported by the NSF (CHE-0446688, OISE-0532040), the Czech Ministry of Education (Kontakt ME857), the EIPAM project sponsored by the European Science Foundation (Grant No. PESC7-20), and the Academy of Sciences of the Czech Republic (Grants No. A100400501 and 1ET400400413). One of us (B.P.) thanks the ESF for the EIPAM Fellowship.

Supporting Information Available: Additional maps of 18 $l2m2$,$l1m1$ pairs of $j_{l2} \cdot Y_{l2m2} \cdot j_{l1} \cdot Y_{l1m1}$ for $l \leq 3$. This material is available free of charge via the Internet at http://pubs.acs.org.

References and Notes

(1) Read, F. H. *J. Phys. B* **1968**, *1*, 893.
(2) Bardsley, J. N.; Mandl, F.; Wood, A. R. *Chem. Phys. Lett.* **1967**, *1*, 359.
(3) Bardsley, J. N.; Read, F. H. *Chem. Phys. Lett.* **1968**, *2*, 333.
(4) Andrick, D.; Read, F. H. *J. Phys. B* **1971**, *4*, 389.
(5) Schulz, G. J. *Rev. Mod. Phys.* **1973**, *45*, 423.
(6) Wong, S. F.; Schulz, G. J. *Phys. Rev. Lett.* **1975**, *35*, 1429.
(7) Gallup, G. A. *J. Chem. Phys.* **1993**, *99*, 827.
(8) Allan, M.; Moreira, O. *J. Phys. B* **2002**, *35*, L37.

(9) Merz, R.; Linder, F. *J. Phys. B* **2003**, *36*, 1143.

(10) Itikawa, Y. *J. Phys. B* **2004**, *37*, R1.

(11) Čurík, R.; Čársky, P. *J. Phys. B* **2003**, *36*, 2165.

(12) Popovič, D. B.; David, D. E.; Michl, J.; Čurík, R.; Čársky, P. *J. Chem. Phys.* **2004**, *121*, 1055.

(13) Itikawa, Y. *Int. Rev. Phys. Chem.* **1997**, *16*, 155.

(14) Frisch, M. J.; Trucks, G. W.; Schlegel, H. B.; Scuseria, G. E.; Robb, M. A.; Cheeseman, J. R.; Zakrzewski, V. G.; Montgomery, J. A., Jr.; Stratmann, R. E.; Burant, J. C.; Dapprich, S.; Millam, J. M.; Daniels, A. D.; Kudin, K. N.; Strain, M. C.; Farkas, O.; Tomasi, J.; Barone, V.; Cossi, M.; Cammi, R.; Mennucci, B.; Pomelli, C.; Adamo, C.; Clifford, S.; Ochterski, J.; Petersson, G. A.; Ayala, P. Y.; Cui, Q.; Morokuma, K.; Malick, D. K.; Rabuck, A. D.; Raghavachari, K.; Foresman, J. B.; Cioslowski, J.; Ortiz, J. V.; Stefanov, B. B.; Liu, G.; Liashenko, A.; Piskorz, P.; Komaromi, I.; Gomperts, R.; Martin, R. L.; Fox, D. J.; Keith, T.; Al-Laham, M. A.; Peng, C. Y.; Nanayakkara, A.; Gonzalez, C.; Challacombe, M.; Gill, P. M. W.; Johnson, B. G.; Chen, W.; Wong, M. W.; Andres, J. L.; Head-Gordon, M.; Replogle, E. S.; Pople, J. A. *Gaussian 98*, revision A.9; Gaussian, Inc.: Pittsburgh, PA, 1998.

(15) Dupuis, M. M.; Farazdel, A.; Karna, S. P.; Maluendes, S. A. *HONDO: A General Atomic and Molecular Electronic Structure System*. In *Modern Techniques in Computational Chemistry: MOTECC-90;* Clementi, E., Ed.; ESCOM Science Publishers: Leiden, The Netherlands, 1990; p 277.

(16) Altmann, S. L. S. L. *Proc. Cambridge Philos. Soc.* **1957**, *53*, 343.